

**Enhanced surface mobility and quantum oscillations in topological insulator
Bi_{1.5}Sb_{0.5}Te_{1.7}Se_{1.3} nanoflakes**

Te-Chih Hsiung, Ding-Yuan Chen, Li Zhao, Yi-Hsin Lin, Chung-Yu Mou, Ting-Kuo Lee, Maw-Kuen Wu, and Yang-Yuan Chen

Citation: *Applied Physics Letters* **103**, 163111 (2013); doi: 10.1063/1.4826092

View online: <http://dx.doi.org/10.1063/1.4826092>

View Table of Contents: <http://scitation.aip.org/content/aip/journal/apl/103/16?ver=pdfcov>

Published by the [AIP Publishing](#)

Advertisement:



Re-register for Table of Content Alerts

Create a profile.



Sign up today!





Enhanced surface mobility and quantum oscillations in topological insulator $\text{Bi}_{1.5}\text{Sb}_{0.5}\text{Te}_{1.7}\text{Se}_{1.3}$ nanoflakes

Te-Chih Hsiung,^{1,2,3,a)} Ding-Yuan Chen,² Li Zhao,² Yi-Hsin Lin,² Chung-Yu Mou,⁴ Ting-Kuo Lee,^{1,2} Maw-Kuen Wu,² and Yang-Yuan Chen^{2,5,a)}

¹Department of Physics, National Taiwan University, Taipei 106, Taiwan

²Institute of Physics, Academia Sinica, Taipei 11529, Taiwan

³Taiwan International Graduate Program, Nano-Science and Technology Program, Institute of Physics, Academia Sinica, Taipei 11529, Taiwan

⁴Department of Physics, National Tsing Hua University, Hsinchu 30013, Taiwan

⁵Graduate Institute of Applied Physics, National Chengchi University, Taipei 116, Taiwan

(Received 7 August 2013; accepted 1 October 2013; published online 16 October 2013)

In this study, a series of $\text{Bi}_{1.5}\text{Sb}_{0.5}\text{Te}_{1.7}\text{Se}_{1.3}$ (BSTS) flakes 80-nm to 140- μm in thickness was fabricated to investigate their metallic surface states. We report the observation of surface-dominated transport in these topological insulator BSTS nanoflakes. The achievement of surface-dominated transport can be attributed to high surface mobility ($\sim 3000 \text{ cm}^2/\text{V s}$) and low bulk mobility ($12 \text{ cm}^2/\text{V s}$). Up to 90% of the total conductance, the surface channel was estimated based on the thickness dependence of electrical conductance and the result of the Shubnikov-de Hass oscillations in a 200-nm BSTS. The nature of nontrivial Dirac surface states was also confirmed by the weak anti-localization effect. © 2013 AIP Publishing LLC. [<http://dx.doi.org/10.1063/1.4826092>]

The recent discovery of topological insulators (TIs) has provided new route for producing low-dimensional relativistic electronic states. The exotic surface states of TIs have attracted the attention of scientists because of their fascinating physical properties and applicability in spintronics and quantum computations.^{1–5} The unique surface states were confirmed by angle-resolved photoemission spectroscopy (ARPES) experiments and scanning tunneling microscopy (STM) on Sb_2Te_3 , Bi_2Te_3 , and Bi_2Se_3 .^{6–11} Magnetotransport studies have also provided a clear picture of the topological surface state and the π Berry phase shift,^{12,13} which gives rise to the immunity of Dirac fermions to localization. Bi_2Te_3 and Bi_2Se_3 are suitable candidates for TI studies because of their large energy gaps. E_g is approximately equal to 0.3 eV and 0.17 eV. However, the metallic bulk conduction of natural imperfections, such as vacancies or antisite defects in these materials, makes it difficult to probe surface Dirac fermions. Therefore, a high-insulating bulk state is a prerequisite for transport property studies of TIs. Substantial effort has made it possible to examine both the surface and the bulk channels either through electrical gating^{13–19} or substitution doping.^{19–22} Recently, it was discovered that $\text{Bi}_{2-x}\text{Sb}_x\text{Te}_{3-y}\text{Se}_y$ (BSTS) is a high-insulating bulk TI. BSTS exhibits a tetradymite structure, a low carrier concentration ($2.3 \times 10^{16} \text{ cm}^{-3}$), and a large bulk resistivity ($8 \Omega \text{ cm}$) because of the ordered occupation of Te/Se in the quintuple-layer unit.^{20,21} However, a reliable detection of surface quantum oscillations is difficult in BSTS flakes because of the inhomogeneous defect²⁰ and low surface mobility.¹⁷ Thus, the low mobility in a bulk channel plays a crucial role in probing surface quantum oscillations.

In this study, we report the observation of surface-dominated transport in the topological insulator BSTS nanoflakes. Shubnikov-de Hass (SdH) oscillations study on the 200-nm BSTS nanoflake indicates that the achievement of surface-dominated transport can be attributed its high surface mobility of $2602 \text{ cm}^2/\text{V s}$ (top surface), $3657 \text{ cm}^2/\text{V s}$ (bottom surface), and low bulk mobility of $12 \text{ cm}^2/\text{V s}$, which is a much lower value than those reported.^{17,18,20,21} Besides, the nontrivial Dirac surface state was further confirmed by the weak anti-localization (WAL) effect and the semiconducting to metallic transport transformation as the thickness of the specimen was reduced to the thin film limit, in which a up to 90% contribution from the surface channel was estimated based on the thickness dependence of the electrical conductance and the result of the SdH oscillations.

BSTS single crystals nominally composed of $\text{Bi}_{1.5}\text{Sb}_{0.5}\text{Te}_{1.7}\text{Se}_{1.3}$ were grown by melting the mixture of Bi (99.999%), Sb (99.999%), Te (99.999%), and Se (99.999%) in sealed evacuated quartz tubes. First the mixture was slowly ramped up to 750°C at a rate of $100^\circ\text{C}/\text{h}$ and kept at 750°C for 12 h. It was then furnace cooled to room temperature at a rate of $100^\circ\text{C}/\text{h}$. The sample was reground and sintered again. The same procedure was repeated three times to ensure sample homogeneity. Finally, the sample was heated to 800°C for 48 h, then cooled to 500°C and annealed for 96 h.

The crystal structures of the samples were identified using powder X-ray diffraction and refined using the General Structure Analysis System (GSAS) software package equipped with the EXPGUI interface, as shown in Fig. 1(a). Transport measurements were conducted using a Quantum Design Physical Property Measurement System (PPMS) and six-terminal Hall bar geometric specimens. The nanoflake specimens were mechanically exfoliated and transferred to the Si_3N_4 (200 nm)/Si substrate. The electrodes of the nanoflake were patterned using standard e-beam lithography and thermal evaporation of Ti/Au.

^{a)}Authors to whom correspondence should be addressed. Electronic addresses: techi@phys.sinica.edu.tw, Tel.: +886 2 2789 8357 and chenyy2@phys.sinica.edu.tw, Tel.: +886 2 2789 6725, Fax: +886 2 2783 4187.

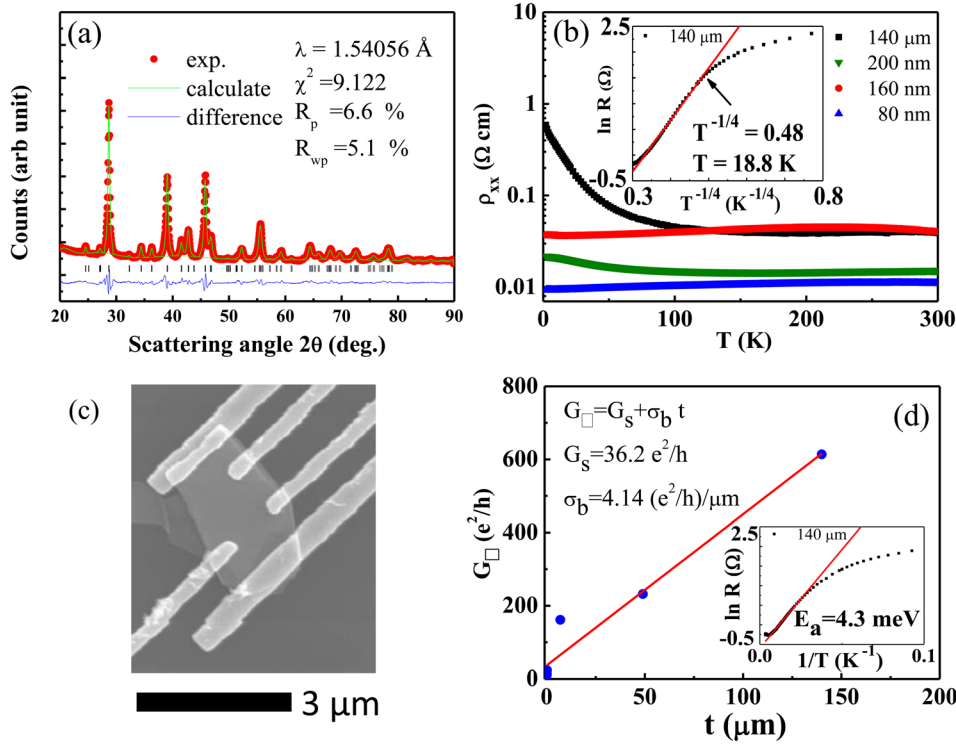


FIG. 1. (a) GSAS refinement of powder X-ray data of a BSTS crystal. Red circles represent experimental results, the green line represents calculated results, the blue line indicates the difference, and the Bragg peaks of the BSTS are shown by the vertical lines, where R_p , R_{wp} , and χ^2 represent the goodness factors. (b) Temperature dependence of resistivity for BSTS specimens with thicknesses of 140 μm , 200 nm, 160 nm, and 80 nm. The inset shows the fit of 3D variable-range hopping to the 140- μm specimens. (c) The SEM image of a BSTS 160-nm nanoflake. (d) Thickness dependence of sheet conductance; the red line is the fit with $G_{\square} = G_s + \sigma_b t$. The inset shows the fitting of the Arrhenius law to the 140- μm specimen.

The considerable thickness dependence of electrical transport showed a transition from semiconducting to metallic behavior as the bulk content is reduced, as shown in Figs. 1(b) and 1(c). For the thick specimens, the thermal activation energies given by the Arrhenius law were 4.3 meV (140 μm), 3.5 meV (49 μm), and 2.37 meV (7 μm). The smaller activation energy of thinner specimens can be explained by the increasing contribution of surface states.^{17,18,20,21} In 140- μm BSTS, a significant deviation occurred below 20 K from the fitting to a three-dimensional variable-range hopping model (3D VRH) with R_{xx} is approximately $\exp[(T/T_0)^{-1/4}]$,²¹ indicating the existence of a parallel metallic conduction of surface states (the inset in Fig. 1(b)). According to Eq. (1), the total conductance G_{\square} of a specimen with a thickness t can be formulated as

$$G_{\square} = G_s + \sigma_b t, \quad (1)$$

where G_s is the surface sheet conductance, and σ_b is the bulk conductivity.^{15,19} $G_s = 36.2$ (e^2/h) and $\sigma_b = 4.14$ (e^2/h) μm^{-1} , which resulted from the fit of thickness dependence of conductance to Eq. (1). For a 200-nm nanoflake at 2 K, up to 90% of the contribution from the surface state was obtained, as shown in Fig. 1(d).

Because successive emptying of Landau levels (LLs) provides the n th minima in ΔR_{xx} , the relation of the LL index n to the Fermi surface cross-section area A_F can be described using the semiclassical Onsager equation: $2\pi(n + \gamma) = A_F \hbar/eB$.

For the Schrodinger electron case, $\gamma = 0$, which results in a zero Berry phase. $\gamma = 1/2$ indicates the case of the Dirac fermion of TIs, which results in a π Berry phase where the charge carrier is immune to localization. The temperature dependence of resistance for a 200-nm nanoflake shows ΔR_{xx} as a function of $1/B$ after a smoothing background subtraction, as shown in Fig. 2(a). Two sets of oscillation periods are

marked; one with a black dashed line ($[\Delta(1/B) = 0.041 \text{ T}^{-1}]$) and the other with a blue dashed line (0.022 T^{-1}) for the surfaces of the nanoflake specimen. The multicomponent nature of SdH oscillations originates from the Fermi-level positions of the two surfaces. If SdH oscillations are as a result of the two-dimensional electron gas (2DEG) formed with band bending near the surface, the corresponding carrier density differs in an order of magnitude¹² compared to the Hall measurement result [$n_{3D} = 3.5 \times 10^{18} \text{ cm}^{-3}$], which is obtained from the fit to low field B ($\pm 1 \text{ T}$) data (Fig. 2(b)).

Fig. 2(c) shows the LL fan diagram plotted in $1/B$ versus n th oscillation minima in ΔR_{xx} . The linear fit of the two-set SdH spectrum yields the intercepts of $\gamma = 0.48 \pm 0.3$ for surface 1 and 0.49 ± 0.02 for surface 2, where γ values are closer to the theoretical value of 0.5 for ideal Dirac fermions. It is assumed that surface 2 is the top surface because environmental contamination provides effective n -type doping²³ to the sample, which strongly influences the top surface. The specimens were closely stacked on the substrate to prevent the bottom surface from air contamination and electron-beam irradiation. Thus, the second set of SdH oscillations appears in the lower inverted field, shown in Fig. 2(a), which was probably from the top surface. In Fig. 2(c), the slope of one set of SdH oscillations provides the cross-section area of the Fermi surface [$A_F = 4.15 \times 10^{17} \text{ m}^{-2}$], and the Fermi wave number was $k_F = 0.0363 \text{ \AA}^{-1}$ and the 2D surface carrier density was $n_{2D} = k_F^2/4\pi = 1.05 \times 10^{12} \text{ cm}^{-2}$ for the top surface (surface 2). The second set of SdH oscillations resulted in $A_F = 2.32 \times 10^{17} \text{ m}^{-2}$ and $k_F = 0.02718 \text{ \AA}^{-1}$, and $n_{2D} = 0.58 \times 10^{12} \text{ cm}^{-2}$ for the bottom surface (surface 1).

Fig. 2(d) shows the fit of temperature dependence of SdH amplitudes to the Lifshitz-Kosevich (LK) theory.^{24,25} The cyclotron mass $m_c = 0.075 m_e$ is the same as that reported.²¹ Once m_c is known, we can calculate the Fermi velocity and the Fermi level position to be $v_F = 5.6 \times 10^5 \text{ m/s}$ and

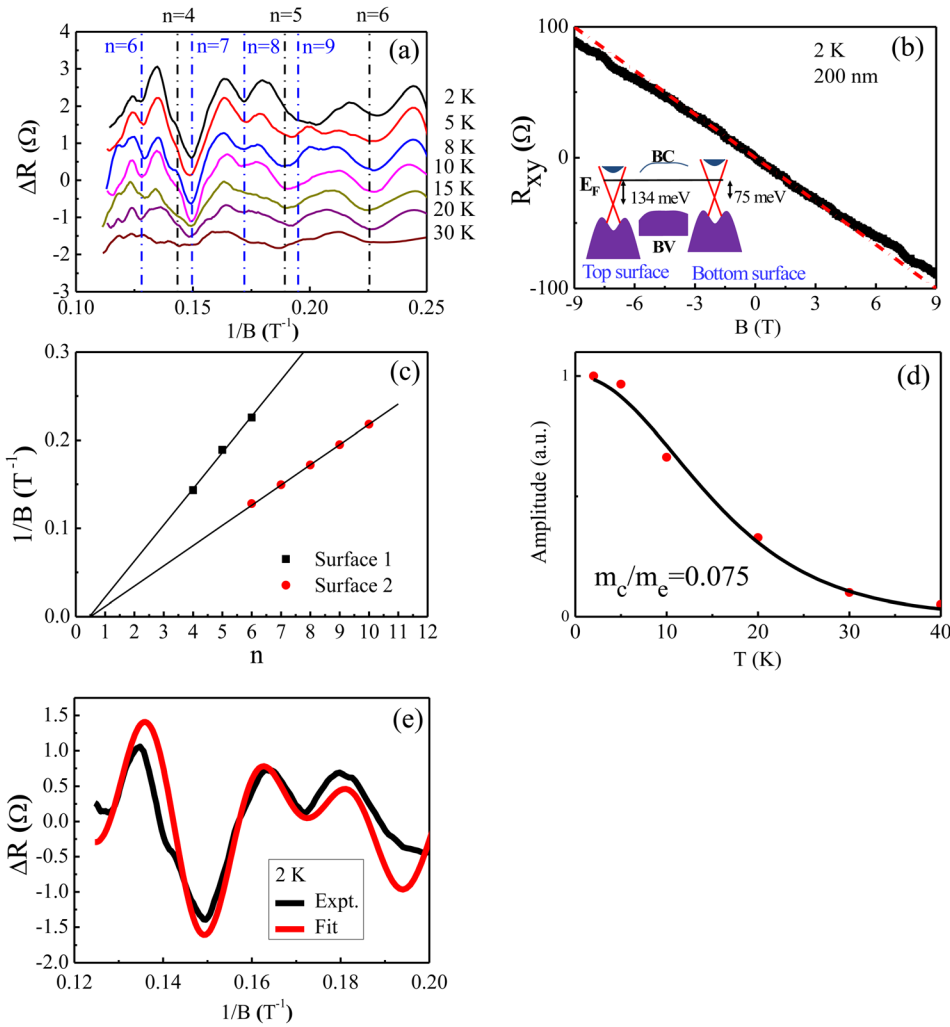


FIG. 2. (a) Temperature dependence of resistance. ΔR_{xx} is function of $1/B$. $n=4, 5$, and 6 are the LLs of the bottom surface; $n=6, 7, 8$, and 9 are the LLs of the top surface of the 200-nm nanoflake. (b) Hall resistance versus magnetic field. The red dashed line is extended from the low B (± 1 T) fit. The inset shows the Fermi level positions of the top and bottom surfaces, respectively. BV is the bulk valance band, and BC is the conduction band. (c) The LL fan diagram plotted in $1/B$ versus the n th oscillation minima in the ΔR_{xx} . (d) The fit of temperature dependence of the SdH oscillation amplitude to the LK theory. (e) ΔR versus $1/B$. The black curve is the experimental data, and the red curve is the fit to LK theory.

$E_F = 134$ meV above the Dirac point for the top surface and $v_F = 4.19 \times 10^5$ m/s and $E_F = 75$ meV for the bottom surface. The high Fermi level position of the top surface is consistent with the results of environmental doping mentioned previously.

Due to the multiple component nature, the Dingle temperature is difficult to extrapolate from the SdH amplitude; therefore, Eq. (2) is used to fit the resistance data to the LK theory

$$\Delta R_{xx}(T, B) \propto \frac{\lambda(T)}{\sinh(\lambda(T))} e^{-\lambda(T_D)} \cos \left[2\pi \left(\frac{F}{B} + \frac{1}{2} + \gamma \right) \right], \quad (2)$$

where F is the frequency of SdH oscillations extracted from the slopes of Fig. 2(c), the thermal factor is $\lambda(T) = \frac{2\pi^2 k_B T}{\hbar e B} m_{cyc}$, and the Dingle temperature is $T_D = \frac{\hbar}{2\pi\tau k_B}$.

The solid red line in Fig. 2(e) shows the optimal fitted results of $\gamma = 0.5$ and $\tau = 1.11 \times 10^{-13}$ s for the top surface, and $\gamma = 0.35$ and $\tau = 1.56 \times 10^{-13}$ s for the bottom surface. The fitted γ values are close to theoretical value of 0.5 for ideal Dirac fermions. According to the Dingle analysis, the scattering time is approximately two to three times larger than that of the bulk BSTS.²¹ Mobility is a measure of scattering time; therefore, it is possible to calculate the surface mobility $\mu_s = 2602 \text{ cm}^2 \text{ V}^{-1} \text{ s}^{-1}$ and the mean free path $\ell = 62$ nm for the top surface, and $\mu_s = 3657 \text{ cm}^2 \text{ V}^{-1} \text{ s}^{-1}$ and $\ell = 65$ nm for the bottom surface. The surface mobility enhancement is consistent with the longer mean free path of the nontrivial topological Dirac state.

The surface contribution to the total conductance ($G_s/G_{\text{tot}} = 84.8\%$) was consistent with the results obtained from the thickness dependence of conductance. Take the

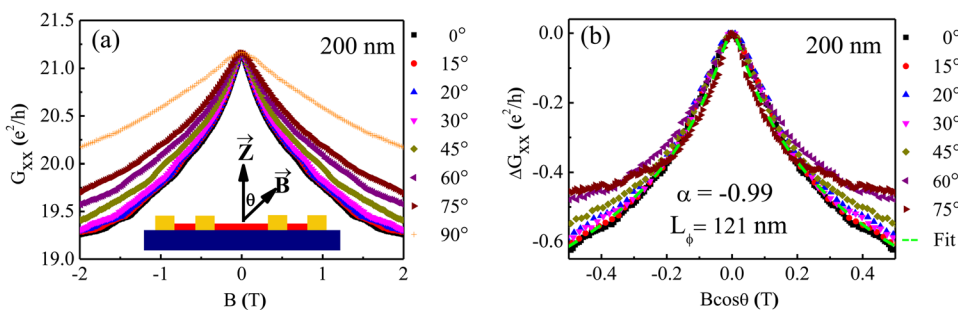


FIG. 3. (a) The angle field dependence magnetoconductance of the 200-nm nanoflake. The inset is a schematic diagram of the measurement. (b) ΔG_{xx} versus the perpendicular field component ($B \cos \theta$) for various angles. Low-angle data merge into a single curve (the green dashed line) fitted using the HLN model.

sheet carrier density into account, $n = n_s + n_b t$.²⁶ The mobility of the bulk channel was $12 \text{ cm}^2/\text{V s}$, which is close to the total Hall mobility of the $140\text{-}\mu\text{m}$ thick BSTS specimen, $13 \text{ cm}^2/\text{V s}$. The low Hall mobility of bulk carriers causes less interference with the surface Dirac fermions; thus, the enhancement of the surface contribution and quantum oscillations was detected in the specimens used in this study.

In addition to SdH oscillations, the helical surface state was further probed using the WAL effect on the 200-nm BSTS. The WAL effect in TIs originated from the π Berry phase, in which the probability of backscattering was suppressed as a result of the destructive interference of time-reversed paths. The angle field dependence magnetoconductance analysis is shown in Fig. 3(a). The sharp cusps of the magnetoconductance in the lower field region are features of WAL. The 2D nature of Dirac fermions associated with the π Berry phase, which is dependent only on the perpendicular component of the applying field, was obtained by subtracting the background from the 3D bulk WAL contribution, $\Delta G_{xx}(\theta, B) = G_{xx}(\theta, B) - G_{xx}(90^\circ, B)$ (5), as shown in Fig. 3(b). Fig. 3(b) shows that low-angle data merge into a single universal curve.¹⁵ The Hikami-Larkin-Nagaoka (HLN) model is used to calculate sheet conductance,²⁷ as given in the following equation:

$$\Delta G_{xx} = -\frac{\alpha e^2}{2\pi^2 \hbar} \left[\ln \left(\frac{\hbar}{4eL_\phi^2 B} \right) - \psi \left(\frac{1}{2} + \frac{\hbar}{4eL_\phi^2 B} \right) \right], \quad (3)$$

where G_{xx} is sheet conductance, L_ϕ is the phase coherent length, and $\psi(x)$ is the digamma function.

The value for α (-0.96) and L_ϕ (121 nm) were obtained for the 200-nm nanoflake. For the WAL effect in TIs, the prefactor α was equal to -0.5 for a single surface state.¹⁷ The complications of topological surface states resulted in an experimental value α between -0.4 and -1.5 .^{15,17} In this study, the value $\alpha = -0.96$ indicated the existence of two surface states.

In this study, dominated surface transport was observed in BSTS nanoflakes. The thickness dependence electrical transport and the SdH oscillations illustrated that the surface states in the 200-nm BSTS nanoflake contribute to nearly 90% of the conductance. The achievement of the surface-dominated transport is mainly attributed to the high surface mobility relative to the bulk channel. The observation of SdH oscillations provides clear evidence of surface Dirac fermions. Surface-dominated transport was further confirmed by the WAL effect showing 2D nature of helical Dirac surface states. Moreover, electrical transport transforms from semiconducting to metallic behavior, and mobility was enhanced when the thickness decreased, indicating that surface states plays a crucial role in the thin film limit. The high-insulating bulk state in BSTS nanoflakes provides opportunities for future quantum computation and spintronics applications.

We would like to thank Hung-Shen Chang, Guang-Yu Guo, and S.-K. Yip for their valuable contributions. This work was supported by the National Science Council, Taiwan, under Grant Number NSC 100-2112-M-001-019-MY3. Technical support was provided by the instrument center and the Core Facilities for Nanoscience and Nanotechnology at the Academia Sinica, Taiwan.

¹J. E. Moore, *Nature (London)* **464**, 194 (2010).

²M. Z. Hasan and C. L. Kane, *Rev. Mod. Phys.* **82**, 3045 (2010).

³X. L. Qi and S. C. Zhang, *Phys. Today* **63**(1), 33 (2010).

⁴L. Fu and C. L. Kane, *Phys. Rev. Lett.* **100**, 096407 (2008).

⁵T. D. Stanescu, J. D. Sau, R. M. Lutchyn, and S. D. Sarma, *Phys. Rev. B* **81**, 241310(R) (2010).

⁶Y. Xia, D. Qian, D. Hsieh, L. Wray, A. Pal, H. Lin, A. Bansil, D. Grauer, Y. S. Hor, R. J. Cava, and M. Z. Hasan, *Nat. Phys.* **5**, 398 (2009).

⁷Y. L. Chen, J. G. Analytis, J. H. Chu, Z. K. Liu, S. K. Mo, X. L. Qi, H. J. Zhang, D. H. Lu, X. Dai, Z. Fang, S. C. Zhang, I. R. Fisher, Z. Hussain, and Z. X. Shen, *Science* **325**, 178 (2009).

⁸D. Hsieh, Y. Xia, D. Qian, L. Wray, F. Meier, J. H. Dil, J. Osterwalder, L. Patthey, A. V. Fedorov, H. Lin, A. Bansil, D. Grauer, Y. S. Hor, R. J. Cava, and M. Z. Hasan, *Phys. Rev. Lett.* **103**, 146401 (2009).

⁹Z. Alpichshev, J. G. Analytis, J.-H. Chu, I. R. Fisher, Y. L. Chen, Z. X. Shen, A. Fang, and A. Kapitulnik, *Phys. Rev. Lett.* **104**, 016401 (2010).

¹⁰T. Zhang, P. Cheng, X. Chen, J. F. Jia, X. C. Ma, K. He, L. L. Wang, H. Zhang, X. Dai, Z. Fang, X. Xie, and Q. K. Xue, *Phys. Rev. Lett.* **103**, 266803 (2009).

¹¹Y. Zhang, K. He, C. Z. Chang, C. L. Song, L. L. Wang, X. Chen, J. F. Jia, Z. Fang, X. Dai, W. Y. Shan, S. Q. Shen, Q. A. Niu, X. L. Qi, S. C. Zhang, X. C. Ma, and Q. K. Xue, *Nat. Phys.* **6**, 584 (2010).

¹²A. A. Taskin, S. Sasaki, K. Segawa, and Y. Ando, *Phys. Rev. Lett.* **109**, 066803 (2012).

¹³A. Roy, S. Guchhait, S. Sonde, R. Dey, T. Pramanik, A. Rai, H. C. P. Movva, L. Colombo, and S. K. Banerjee, *Appl. Phys. Lett.* **102**, 163118 (2013).

¹⁴B. F. Gao, P. Gehring, M. Burghard, and K. Kern, *Appl. Phys. Lett.* **100**, 212402 (2012).

¹⁵J. Chen, X. Y. He, K. H. Wu, Z. Q. Ji, L. Lu, J. R. Shi, J. H. Smet, and Y. Q. Li, *Phys. Rev. B* **83**, 241304 (2011).

¹⁶F. Xiu, L. He, Y. Wang, L. Cheng, L.-T. Chang, M. Lang, G. Huang, X. Kou, Y. Zhou, X. Jiang, Z. Chen, J. Zou, A. Shailos, and K. L. Wang, *Nat. Nanotechnol.* **6**, 216 (2011).

¹⁷J. Lee, J. Park, J. H. Lee, J. S. Kim, and H. J. Lee, *Phys. Rev. B* **86**, 245321 (2012).

¹⁸B. Xia, P. Ren, A. Sulaev, P. Liu, S. Q. Shen, and L. Wang, *Phys. Rev. B* **87**, 085442 (2013).

¹⁹X. Y. He, T. Guan, X. X. Wang, B. J. Feng, P. Cheng, L. Chen, Y. Q. Li, and K. H. Wu, *Appl. Phys. Lett.* **101**, 123111 (2012).

²⁰Z. Ren, A. A. Taskin, S. Sasaki, K. Segawa, and Y. Ando, *Phys. Rev. B* **84**, 165311 (2011).

²¹A. A. Taskin, Z. Ren, S. Sasaki, K. Segawa, and Y. Ando, *Phys. Rev. Lett.* **107**, 016801 (2011).

²²T. Arakane, T. Sato, S. Souma, K. Kosaka, K. Nakayama, M. Komatsu, T. Takahashi, Z. Ren, K. Segawa, and Y. Ando, *Nature Commun.* **3**, 636 (2012).

²³L. Fang, Y. Jia, D. J. Miller, M. L. Latimer, Z. L. Xiao, U. Welp, G. W. Crabtree, and W. K. Kwok, *Nano Lett.* **12**, 6164 (2012).

²⁴D. Schoenberg, *Magnetic Oscillations in Metals* (Cambridge University Press, London, 1984).

²⁵D. X. Qu, Y. S. Hor, J. Xiong, R. J. Cava, and N. P. Ong, *Science* **329**, 821 (2010).

²⁶Y. S. Kim, M. Brahlek, N. Bansal, E. Edrey, G. A. Kapilevich, K. Iida, M. Tanimura, Y. Horibe, S. W. Cheong, and S. Oh, *Phys. Rev. B* **84**, 073109 (2011).

²⁷S. Hikami, A. I. Larkin, and Y. Nagaoka, *Prog. Theor. Phys.* **63**, 707 (1980).